

QUANTITATIVE ANALYSIS OF SILICA NANOPARTICLE STRUCTURES VIA  
SMALL-ANGLE X-RAY SCATTERING

A Thesis

Presented to the Faculty of the Graduate School

of Cornell University

In Partial Fulfillment of the Requirements for the Degree of

Master of Science

by

Alvin Chang

August 2022

© 2022 Alvin Chang

## ABSTRACT

Ultrasmall nanoparticles have seen growing interest in several fields such as medicine, optics, and catalysis due to their unique size-dependent properties. Among these are fluorescent core-shell silica nanoparticles synthesized in water known as Cornell prime dots (C' dots), which are composed of a silica core and a poly(ethylene glycol) (PEG) shell. These C' dots are poised to become promising diagnostic and therapeutic tools in medicine, particularly for cancer applications. While spherical C' dots have already been in FDA-approved human clinical trials, exploration has expanded into different topologies of silica nanoparticles such as rings and cages, providing higher aspect ratios and higher surface area to volume ratios.

For clinical translation of such nanostructures, quantitative assessments of their size and size dispersity remain parameters for further investigation and are critical to understanding and evaluating their effectiveness and safety in nanomedicine applications. Here, solution small-angle X-ray scattering was employed to characterize 3D structural details of ring-type silica nanostructures and their size and size dispersity. A hollow cylinder model provided consistent structural and dispersity parameters that were supported by transmission electron microscopy investigations.

## BIOGRAPHICAL SKETCH

Alvin Chang was born in Gainesville, FL, but was raised in Corvallis, Oregon. He graduated from Oregon State University with degrees in Chemical Engineering and Bioengineering in 2019. In 2020, he joined the Ulrich Wiesner lab in the department of Materials Science and Engineering at Cornell University and focused on quantifying size dispersions and characterization for silica nanoparticles. He will graduate with a Masters of Science in 2022.

## ACKNOWLEDGMENTS

I would like to thank my parents, family, Professor Uli Wiesner, and Professor Lara Estroff. I would also like to thank all of the Wiesner group members, especially Jacob and Rachel. Special thanks also goes out to Konrad, Dana, Fei, and William. I would also like to thank all members of CHESS, especially Dr. Richard Gilligan and Qingqui Huang. Finally, I would like to thank the NSF Graduate Research Fellowships Program for funding of this project.

## TABLE OF CONTENTS

Biographical Sketch	iv
Dedication	v
Acknowledgements	vi
Table of Contents	vii
List of Figures	viii
<b>CHAPTER 1</b>	
INTRODUCTION	1
1.1 Ultrasmall Silica Nanoparticles	1
1.1.2 Mesoporous Silica Nanoparticles	2
1.2 Quantitative Measurements of Size Dispersity in Silica Nanoparticles	3
1.3 Small Angle X-Ray Scattering	5
1.4 Organization of the Thesis	5

<b>CHAPTER 2</b>	
MATERIALS AND METHODS USED TO SYNTHESIZE MESOPOROUS C DOTS AND C-RINGS	6
2.1 Materials	6
2.2 Methods	7
2.2.1 Synthesis of the Particles	7
2.2.2 Purification of the Particles	8
2.2.3 TEM Characterization of Particle Morphology and Size	9
2.2.4 Characterization of Particles from Optical Properties	10
2.2.5 SAXS Characterization of Particles	10
<b>CHAPTER 3</b>	
RESULTS AND DISCUSSION	13
3.1 Determination of a Suitable Form Factor	13
3.2 Validation of Specific SAXS derived Structural Parameters via TEM	22
<b>CHAPTER 4</b>	
CONCLUSION	33
<b>CHAPTER 5</b>	
SUPPLEMENTARY INFORMATION	34
REFERENCES	40

## LIST OF FIGURES

Figure 1: Schematic of synthesis protocol to fabricate C-rings.....	14
Figure 2: Schematic of torus model and simulation and best fit with their parameters of Sample 1 using the torus model.....	17
Figure 3: Schematic of hollow cylinder model and simulation and best fit with their parameters of Sample 1 using the hollow cylinder model. Guinier analysis of Sample 1 is also given.....	19
Figure 4: Scattering patterns, Guinier analyses, and best fits of Samples 2, 3, 4, and 5.....	22
Figure 5: TEM images of Samples 2, 3, 4, and 5 with plots comparing parameters from TEM and SAXS.....	25
Figure 6: Scattering pattern of mC dot, Rings, and Bimodal samples with their Guinier analyses and best fits.....	30
Figure 7: TEM image of mC dot sample with plot comparing TEM and SAXS values as well as histograms of TEM-determined parameters.....	32
Figure S1: Additional scattering patterns of Samples 4 and 5.....	36

Figure S2: Additional scattering patterns of mC dots, Bimodal, and Rings.....36

Figure S3: Pair distance distribution function plots of mC dots, Bimodal,  
and Rings.....37

Figure S4: TEM image of Bimodal sample with plot comparing TEM and SAXS  
values as well as histogram of TEM-determined parameters.....38

LIST OF TABLES

Table 1: PEGylations and functionalizations of all samples.....20

Table 2: SAXS parameters from Samples 2, 3, 4, and 5.....22

Table 3: SAXS and model-independent Guinier parameters of mC dot, Rings, and  
Bimodal samples.....30

# CHAPTER 1

## INTRODUCTION

### 1.1 Ultrasmall Silica Nanoparticles

Ultrasmall inorganic nanoparticles have been the recipients of growing interest in several burgeoning fields such as medicine, optics, and catalysis due to their unique size-dependent properties<sup>1-7</sup>. However, a key weakness hindering the vast potential of these particles is their susceptibility to aggregation and to protein adsorption within the bloodstream. To work around these issues, particles are often coated with an organic outer layer to create an organic-inorganic core-shell particle. A particular surface layer composition that has emerged in medical applications is the inert polymer poly(ethylene glycol) (PEG), which serves to sterically shield the inorganic core from interactions with each other (colloidal stability) as well as with components within the bloodstream (e.g., preventing protein corona formation)<sup>8-10</sup>.

One such organic-inorganic core-shell particle that has extraordinary promise in medicine as both a diagnostic and therapeutic tool are Cornell prime dots (C' dots)<sup>11</sup>. C' dots synthesized in aqueous solutions are fluorescent silica particles coated with an outer PEG layer and have been approved by the FDA for human clinical trials<sup>12,13</sup>. So far, C' dots have been used for detection and bioimaging of cancer<sup>13-15</sup>, and show promise in drug delivery and therapeutics<sup>14, 16-21</sup>. Their key advantage lies in their sub-10 nm size, which grants them renal clearance -- rapid

clearance through the kidneys and into the bladder of an organism, enabling a “target-or-clear” approach where C’ dots either target the site of disease or get efficiently cleared out of the body, leading to favorable biodistributions<sup>22-24</sup>. Additionally, the silica chemistry allows for facile functionalization, e.g. with targeting moieties that can be used for detection and imaging<sup>25</sup>.

### **1.1.2 Mesoporous Silica Nanoparticles**

In 1992, discovery of MCM-41 materials with pore sizes varying from 15-100 Angstroms<sup>26</sup> saw great potential in drug delivery and biosensor applications and opened the door towards the formation and application of mesoporous silica nanoparticles (MSNs) synthesized through silica and micelle interactions for biomedical applications<sup>27-29</sup>. Since then, development of mesoporous materials has only shifted towards smaller scales, eventually pushing into the sub-10 nm regime of C dots with the goal to enable efficient renal clearance.

The Wiesner group has recently expanded into mesoporous silica nanoparticles with the development of single-pore mesoporous C dots (mC dots), rings referred to as C rings, and cages<sup>30-33</sup>. These alternative morphologies all take advantage of silica and micelle interactions and typically employ cetyltrimethyl ammonium bromide (CTAB) as the surfactant template, trimethyl benzene (TMB) as the pore expander, tetramethoxy-silane (TMOS) as the silica source, 7-diethylaminocoumarin-3-carboxylic acid (DEAC) as the fluorescent dye, and PEG as the organic passivating shell.

These morphologies of silica nanoparticles offer the advantage of increased surface area over C dots, allowing for higher drug loading capacity which could be advantages in particular for therapeutic purposes. Having two distinct surfaces (inner and outer) in these morphologies also opens the possibility of functionalizing both surfaces with different chemistries, allowing for the development of multifunctional tools<sup>34</sup>.

## **1.2 Quantitative Measurements of Size Dispersity in Silica**

### **Nanoparticles**

For both C dots and their mesoporous counterparts, which can be applied to clinical settings, it is critical that the particles are quantitatively and comprehensively characterized. Key parameters include the size and size distributions of the particles to maximize chances that they can safely undergo renal clearance. Many nanoparticle syntheses suffer from poor dispersity or aggregation issues which can occur in either the synthesis or purification steps. For particles to undergo renal clearance, they must meet the strict requirement of sub-10 nm sizes. Rather than just optimizing for a low mean particle size, it is especially important to ensure that particles have a narrow size distribution to avoid a significant population of particles being above the renal cutoff. Thus, it is highly desirable to quantitatively assay size and size distributions of the ultrasmall nanoparticles with new topologies like rings.

Common characterization techniques for C' dots include fluorescence correlation spectroscopy (FCS), transmission electron microscopy (TEM), and dynamic light scattering (DLS). FCS is a technique which takes advantage of the fluorescent dye in the nanoparticles in order to increase signal-to-noise relative to DLS in the estimate of the hydrodynamic radii of ultrasmall particles. Analysis typically relies on the Stokes-Einstein relation, however, which assumes a spherical particle shape. For nonspherical morphologies like C rings, these estimates are not expected to be accurate. In addition, FCS is only sensitive to dye-containing particles, so it may leave out subpopulations of dye-free particles. Although TEM can create a clear visual of the particles' size and size dispersity, only the high contrast silica cores are observed while the polymer corona is not. Furthermore, in particular for the case of ultrasmall particle sizes degradation under the electron beam may influence the results. DLS is a simple and facile method for size distribution characterization, but as stated earlier its sensitivity goes down markedly as particle sizes become ultrasmall. Furthermore, the fluorescence of C' dots encapsulating red dyes overlaps with the scattered laser signal, excluding such C' dots from its analysis.

As a result, for C' dots, small angle X-ray scattering (SAXS) has emerged as an excellent tool to quantify particle size dispersities. This was demonstrated by Barteau et al., who characterized the size and size distributions of a number of spherical C' dot compositions and sizes using quantitative form factor analysis based on SAXS data sets<sup>35</sup>. In contrast, to the best of our knowledge SAXS

analysis of other ultrasmall silica nanoparticle topologies like silica rings (C rings) or mC dots has not been described before.

### **1.3 Small Angle X-ray Scattering**

SAXS is an analytical technique that can provide ensemble measurements of particle system sizes and shapes in the 1-100 nm size range. It is fast, accurate, non-destructive, and requires little sample preparation while being very versatile in that it can study all three states of matter, i.e. solids, liquids, and gases. The SAXS experiments described here utilize synchrotron X-rays. The high flux X-ray beams lead to high signal-to-noise ratios, enabling detailed structural analysis via comparison with form factor models of nanoparticles. To date, SAXS has already been applied to a broad range of materials of study including inorganic nanoparticles, biological materials, polymers, and colloids<sup>36-38</sup>.

### **1.4 Organization of this Thesis**

This thesis presents the quantitative analysis of silica nanostructures with ring-type morphologies referred to as C rings and mC dots. Beyond the necessary background provided in this chapter 1, in chapter 2 the materials and methods employed are detailed. In chapter 3, results of SAXS experiments conducted on C rings and mC dots are described, analyzed, and discussed. In chapter 4, the work is summarized, and conclusions are provided, e.g., about possible future directions of the work. Finally, chapter 5 contains additional supplementary information.

## CHAPTER 2

# MATERIALS AND METHODS USED TO SYNTHESIZE AND CHARACTERIZE MESOPOROUS C DOTS AND C- RINGS

### 2.1 Materials

All materials were used as received. Hexadecyltrimethyl ammonium bromide (CTAB,  $\geq 99\%$ ), tetraethyl orthosilicate (TMOS,  $\geq 99\%$ ), 2.0M ammonium hydroxide in ethanol, (3-Aminopropyl)trimethoxysilane (APTMS, 97%) and anhydrous dimethyl sulfoxide (DMSO,  $\geq 99\%$ ) were purchased from Sigma Aldrich. 2-[methoxy(polyethyleneoxy)6-9propyl]trimethoxysilane (PEG-Silane, MW ~500), and (3-mercaptopropyl) trimethoxysilane (MPTMS, 95%) were obtained from Gelest. Mesitylene (TMB, 99% extra pure) were purchased from Acros Organics. [7-Diethylaminocoumarin-3-carboxylic acid, succinimidyl ester] (DEAC, SE) was purchased from ChemCruz. Absolute anhydrous ethanol (200 proof) was obtained from Koptec. Deferoxamine-Bn-NCS (DFO-NCS, 94%) was purchased from Macrocyclics. Glacial acetic acid was purchased from EMD Millipore Corporation. 0.9% sodium chloride irrigation USP solution was purchased from ChemCruz. Syringe filters (0.22  $\mu\text{m}$ , PTFE membrane) were purchased from Foxx Life Science. Vivaspin sample concentrators (MWCO 30K) and Superdex 200 prep grade were obtained from GE Health Care. Snake Skin dialysis membrane (MWCO 10K) were purchased from Thermo Fisher Scientific.

Deionized (DI) water was generated using Millipore Milli-Q system (18.2 M $\Omega$ .cm).

## **2.2 Methods**

### **2.2.1 Synthesis of the Particles**

In this thesis two types of silica nanoparticles were investigated, i.e., C-rings and mC dots, that were synthesized as described in literature<sup>30,31,33</sup>. Briefly, 0.227 mmol of CTAB and 1 mL of 20 mM aqueous ammonium hydroxide solution were added into 9 mL DI water. There was no addition of TMB following this step for the synthesis of mC dots, whereas the concentration of TMB was varied from 36-144 mM to synthesize C-rings of varying diameters. The solution was then stirred for approximately 24 hrs at 30 °C to fully dissolve the CTAB. Next, 0.45 mmol TMOS and 0.000135 mmol DEAC dye (conjugated 18-20 h prior to addition with 0.01 mmol APTES in DMSO) were added into the reaction under stirring. The solution was kept stirred at 30 °C for 24 h. Then, 0.21 mmol PEG-silane was added into the solution and stirring continued for another 24 h and 30 °C to quench the particle growth. The sample was then heated at 80 °C for 24 h without stirring to finalize covalent attachment of the PEG-silane functional groups onto the silica nanoparticle (SNP) surface. The relative molar ratios of the reactants were 1 TMOS: 0.498 CTAB: 0.043 ammonium hydroxide: (0-3.12) TMB: 0.47 PEG-Silane: 0.003 DEAC: 0.022 APTES: 1090.9 DI water. The synthesis of mC dots and C-rings follow nearly the same protocol, differing only in the amount of TMB used (mC dot synthesis used 0 mM TMB whereas C-ring synthesis used concentrations of TMB ranging from 60-144 mM).

Next, the solution was cooled down to room temperature and then transferred into a dialysis membrane. The solution was dialyzed three times for 24 h in an acetic acid solution composed of ethanol, DI water, and glacial acetic acid (volume ratio 1:1:0.014) to etch away the CTAB. After acetic acid dialysis, the solution was dialyzed three times in 1L of DI water for 24 h. Next, the solution was syringe filtered (0.2  $\mu\text{m}$  MWCO) to remove large aggregates. For particles with DFO chelator functionalization, following dialysis, the solution was transferred back into a flask where 2  $\mu\text{L}$  of APTMS was added into the reaction at 600 rpm at room temperature. Next, 0.42 mmol of DFO-NCS chelator was added to the solutions where they react with the primary amines on the nanoring surface via amine-NCCS conjugation. The solution was then heated at 80° C overnight. DFO functionalized rings had relative molar ratios of 1 TMOS: 0.498 CTAB: 0.043 ammonium hydroxide: (0-3.12) TMB: 0.47 PEG-Silane: 0.003 DEAC: 0.022 APTES: 0.05 APTMS:1.83 DFO-NCS: 1090.9 DI water.

### **2.2.2 Purification of the Particles**

To purify the particles, sample solution was transferred from the dialysis membrane into spin filter sample concentrators and centrifugation was performed in an Eppendorf 5810 R at 2500 RPM for 30 min. Next, ~1 mL of up-concentrated samples were injected into a GPC column packed with Superdex 200 prep grade resin. Buffer solution (0.9% sodium chloride) was pumped into the column by a Bio-Rad BioLogic LP system. Bio-Rad BioFrac fraction collector

collected GPC fractions of samples. After fractionation, particle products were separated from particle aggregates and reaction precursors (e.g. free dye-silanes) by collecting the full-width half-max of the product peak in the elution profile. The purified particles were then transferred back into spin filters and were centrifuged at 2500 RPM for 25 min.

### **2.2.3 TEM Characterization of Particle Morphology and Size**

To prepare particles for TEM, first the sample solution (5-15  $\mu\text{M}$  concentration) was diluted by adding 3  $\mu\text{L}$  of solution into 100  $\mu\text{L}$  of either DI water or ethanol. Next, one droplet (15-30  $\mu\text{L}$ ) of the diluted solution is dropped using a 100  $\mu\text{L}$  pipette onto a carbon-coated copper grid, which is placed on a filter paper. Once the droplet is dropped, the grid is put back into the grid box and the remaining solution is evaporated at room temperature. TEM images were taken using a FEI F20 STEM/TEM operated at an acceleration voltage of 120kV. To analyze particle size and distribution, processed images were exported to ImageJ. In the ImageJ software, at least 50 particles were measured using the straight segment function. Particle inner radius and outer radius were measured. For every porous particle/ring that was measured, four measurements across the particle were taken. Particles that were on the edge of the image were not used and if particles were overlaid on top of each other, only the top particle was measured.

## 2.2.4 Characterization of Particles from Optical Properties

All of the samples and free dye were absorption matched by dilution into DI water. Varian Cary 5000 spectrophotometer (Varian, Inc., Palo Alto, CA) was employed to measure and match the absorption spectra of each sample. Extinction coefficient of DEAC ( $34000 \text{ M}^{-1} \text{ cm}^{-1}$ ) and concentration information obtained from separate fluorescence correlation spectroscopy (FCS) measurements was used to calculate the number of dyes encapsulated in the samples.

## 2.2.5 SAXS Characterization of Particles

Sample solutions were diluted to concentrations at 1, 3, 5, 10, 20, and 50  $\mu\text{M}$  in DI water. As the stock solutions had been filtered before synthesis, they were not refiltered prior to SAXS measurements.

Static SAXS measurements on sample solutions were performed at the Cornell High Energy Synchrotron Source (CHESS) G1 station using an X-ray beam ranging from 7-14 keV. SAXS curves were collected on a PILATUS 300K (Dectris) detector at sample-to-detector distance of 1650 mm, yielding a q-range of  $0.007\text{-}0.25 \text{ \AA}^{-1}$ . Data reduction and analysis of the scattering curves were performed by NIKA<sup>39</sup>. SAXS measurements using an oscillatory flow cell were taken at the MacCHESS BIOSAXS station (station G1)<sup>40-41</sup>. Samples were measured for 10 seconds, with frames collected every second and then averaged over the entire time range. Background solution of DI water was measured before each sample measurement for 10 seconds at one second frames. Background

scattering was then subtracted from the measured sample scattering to produce final background-subtracted scattering curves. BIOXTAS RAW was used to perform model independent analysis such as Guinier fitting and GNOM pair distribution function (PDF) fitting<sup>42-43</sup>.

Guinier fitting employs Guinier's approximation which states that at low-q regions, the scattering profile can be approximated by Equation 1<sup>44</sup>:

$$I(q) \approx I(0)e^{-q^2 R_g^2/3} \quad (\text{Equation 1})$$

where  $R_g$  is the radius of gyration and  $I(0)$  is the intensity at zero scattering angle ( $q=0$ ). Taking the natural log of the equation produces a linear plot comparing  $\ln(I)$  vs  $q^2$ . This is referred to as the Guinier plot and provides information on the size of the molecule and, often more importantly, on the quality of the SAXS data as many data collection problems such as aggregation and interparticle interactions are highlighted in the low  $q$  region and will be displayed in the Guinier plot as a deviation from linearity<sup>44</sup>.

Obtaining the pair distance distribution function analysis requires applying a Fourier transform to the experimental data. Initially, the output scattering profile is measured in reciprocal distance space and  $I(q)$  has units of one over distance. Thus, applying a Fourier transformation can get real space information about the sample, using Equation 2:

$$P(r) = \frac{r^2}{2\pi^2} \int_0^\infty q^2 I(q) \frac{\sin(qr)}{qr} dq \quad (\text{Equation 2})$$

This function is referred to as the pair distance distribution function and is essentially the  $r^2$  weighted histogram of all possible pairs of electrons in the

sample. However, Equation 2 cannot be used to directly calculate the P(r) function as I(q) data is only available at discrete points over a limited q-range, and noise from the measurements can affect the function. To work around this complication, the P(r) function is instead fit against the scattering pattern using Equation 3:

$$I(q) = 4\pi \int_0^{D_{max}} P(r) \frac{\sin(qr)}{qr} dr \quad (\text{Equation 3})$$

The best fit P(r) function will then yield valuable information such as the radius of gyration, and a distribution of the electron pairs in the sample, revealing insight into the shape of the sample. All fits of the P(r) function were performed by the GNOM software in the ATSAS package used in BioSAXS RAW<sup>45</sup>.

Model dependent fitting and analysis were performed using SasView (v. 5.0.3) and SASfit<sup>46-47</sup>. Form factor fits to the scattering data were minimized using Levenberg-Marquardt nonlinear least-squares regression. Further estimation of parameter uncertainty was carried out using the DREAM algorithm (Markov Chain Monte Carlo sampling)<sup>48</sup>.

# CHAPTER 3

## RESULTS AND DISCUSSION

### 3.1 Determination of a Suitable Form Factor

In this study, a total of eight different C-ring and mC dot particles were measured with SAXS under a concentration ranging from 1 to 10  $\mu\text{M}$ . There was a total of six C-ring samples (referred to as Samples 1-5 and Rings), one mC dot sample (mC dots), and one bimodal morphology sample (Bimodal). One C-ring sample was inner and outer PEGylated and functionalized with DFO (Sample 1), two samples were inner and outer PEGylated (Samples 2-3), and three samples were outer PEGylated (Samples 4-5, Rings). Once SAXS scattering patterns were collected, the lowest concentration that yielded high signal to noise ratios throughout the entire  $q$  range was chosen for study and fitting. In the fitting process, first a form factor that could properly fit the scattering patterns was looked for. A number of form factors were tested to fit the samples and the form factor that produced the best fits will be discussed. In fitting the samples, first previous TEM measurements were used as initial parameters in the form factor. This is done to put the values for the fit in a realistic range, minimizing the potential of the fit falling into local minimum. Next, the scaling parameter and the background were determined by fitting over the low- $q$  range of the curve. The background was held constant and was set to the scattering intensity at the highest  $q$  values. Size and shape parameters in the form factor were held constant and only the scaling parameter was fit for over this region. The shape and size of the

samples are then fit for by extending the range of the fit to the central- $q$  region. Finally, once the parameters for the form factor have been optimized, polydispersity is considered as well and the scattering pattern is fit over the entire  $q$  range while fitting for all the shape parameters and polydispersity. SAXS fitting results are then compared to TEM measurements to test the fit values.

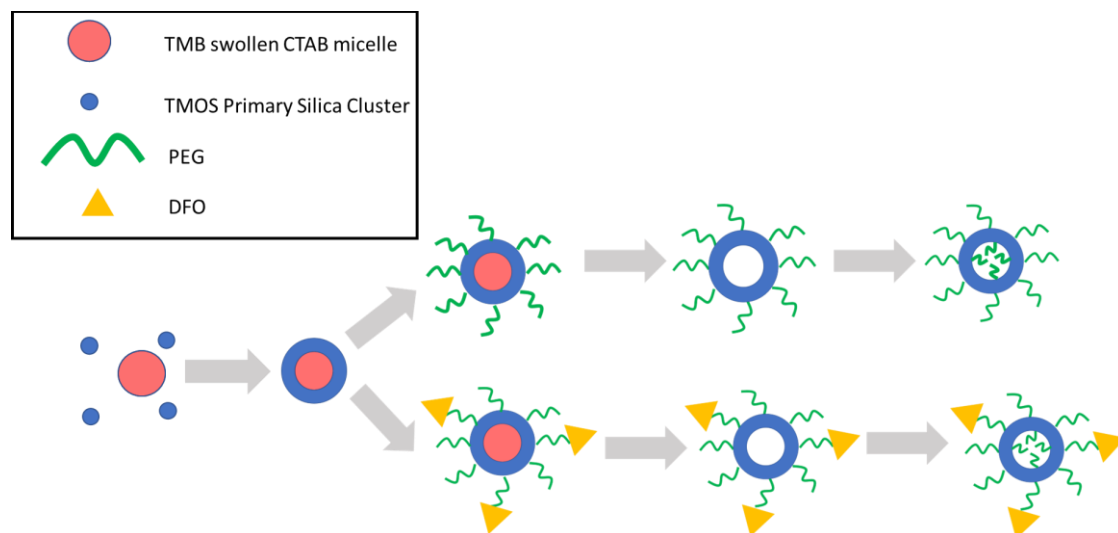


Figure 1: Synthesis scheme of C-rings. The protocol for mC dots is the same except without TMB. Initially, primary silica clusters descend onto the CTAB micelle to form a ring-like shape around the micelle. Next, the outer surface is functionalized with PEG and can also be functionalized with DFO. Afterwards, the CTAB micelle is removed and the inner surface can be PEGylated.

Initially, SAXS measurements were taken on only one ring sample synthesized from TMOS/CTAB/TMB relative molar ratios of 1/0.5/1.56. The outer surface was functionalized with 6EO-PEG-Silane, 7-Diethylaminocoumarin-3-carboxylic acid (DEAC) dye, and chelator desferoxamine (DFO) in the presence of CTAB micelles, while the inner surface was functionalized with 3EO-PEG-silane after CTAB removal (Figure 1). This sample was synthesized by Melik Turker and will be referred to as Sample 1. SAXS of Sample 1 shows a curve with little oscillations, suggesting a polydisperse sample (Figure 2b). In addition, in the

middle  $q$  region, the curve descends with a power law decay between that of a spherical and cylindrical shape. An upturn at low  $q$  values also suggests aggregation or interparticle attractions. To find a suitable form factor for the fit, first a torus with elliptical shell form factor from SASfit was used to analyze the scattering patterns, as shown in Figure 2a. In this model, key parameters are  $R$ ,  $a$ ,  $\Delta a$ ,  $\nu$ ,  $\eta_c$ ,  $\eta_{sh}$ , and  $\eta_{sol}$ , where  $R$  is the radius of revolution (measured from the center of the torus to the center of the ring of the torus),  $a$  is the inner radius (measured from the center of the torus to the inner ring of the torus),  $\Delta a$  is the thickness of the outer layer,  $\nu$  is the aspect ratio of the torus (which is dependent on the  $a + \Delta a$  ratios between the revolved circle or ellipse forming the torus), and  $\eta_c$ ,  $\eta_{sh}$ , and  $\eta_{sol}$  are the scattering length densities of the core, shell, and solution, respectively.

Initial parameters for the curve fitting were determined by previous measurements described in literature detailing syntheses and TEM analyses of the rings<sup>33</sup>.

Parameters used were a  $R$  of 3.9 nm,  $a$  of 0.8 nm,  $\Delta a$  of 0.8 nm,  $\nu$  of 1,  $\eta_c$ ,  $\eta_{sh}$ , and  $\eta_{sol}$  of  $16.5 \times 10^{-6} \text{ \AA}^{-2}$ ,  $10.5 \times 10^{-6} \text{ \AA}^{-2}$ , and  $9.45 \times 10^{-6} \text{ \AA}^{-2}$ , respectively. The scattering length density of the core and the shell were taken from previous studies,<sup>35</sup> and the scattering length density of water is a well-known value. To get the value for amorphous silica nanoparticles, it was known that amorphous silica nanoparticles had a density in the range of 1.6-2.1  $\text{g/cm}^3$ , so an intermediate density of 1.9-1.95  $\text{g/cm}^3$  was assumed, yielding the scattering length density of  $16.5 \times 10^{-6} \text{ \AA}^{-2}$ . The density of PEG ranged between 9.56 and 10.59, so an intermediate value was

chosen for this fit<sup>35</sup>. Using the previously-mentioned parameters, a scattering curve was simulated and was compared to the experimental scattering curve in Figure 2b. Clearly, the initial parameters of the model do not provide an accurate fit of the experimental curve. Next, the model was allowed to fit to its lowest least-squares regression value, with results shown in Figure 2c. This fit yielded the following parameters: R: 3.91 nm, a: 1.07 nm,  $\Delta a$ : 0 nm,  $\nu$ : 3.8, and  $\eta_c$ ,  $\eta_{sh}$ , and  $\eta_{sol}$  equal to  $16.5 \cdot 10^{-6} \text{ \AA}^{-2}$ ,  $10.5 \cdot 10^{-6} \text{ \AA}^{-2}$ , and  $9.45 \cdot 10^{-6} \text{ \AA}^{-2}$ , respectively. This yields the physical dimensions of an inner radius of 2.84 nm and inner diameter of 5.68 nm and an outer radius of 4.98 nm and outer diameter of 9.96 nm and a height of 8.132 nm. The inner radius is the distance from the center of the ring to the inner edge of the ring and is given by  $R-a$  and the outer radius is the distance from the center of the ring to the outer edge of the ring and is given by  $R+a+\Delta a$ . Although the resulting fit is better than that using the starting values, and the parameters obtained from the fit translate over to realistic physical dimensions, the fit still does substantially deviate from the measured data. Furthermore, the height is substantially above the expected  $\sim 2$  nm size of a primary silica cluster making up the ring structure<sup>33</sup>. The poor quality fit, in particular at larger scattering vector,  $q$ , is likely because the torus with elliptical shell form factor in SASfit could only fit the scattering curve using a monodisperse approximation, meaning that it assumed that all the particles in the sample had equivalent physical dimensions. This is a common problem with more complicated form factors such as the torus with an elliptical shell, and previous literature has stated that there is no existing software that can accommodate

polydispersities in even a torus (without a shell) form factor<sup>49</sup>. However, a quick look at the scattering pattern would suggest that the sample has a clear size distribution in at least one parameter, as the distinct features of a monodisperse form factor, like the oscillations at larger scattering vector,  $q$ , are missing in the measured data set. Instead, the scattering intensity monotonically decreases with increasing  $q$ , clearly suggesting a polydisperse sample. Additionally, from previous studies we know there is a clear distribution, e.g., around in the inner and outer diameters of ring samples, as measured by TEM, lending support to the polydisperse nature of the sample<sup>33</sup>. As such, it was clear that future fitting analysis needed a new form factor or software that could accommodate polydispersity in the fits.

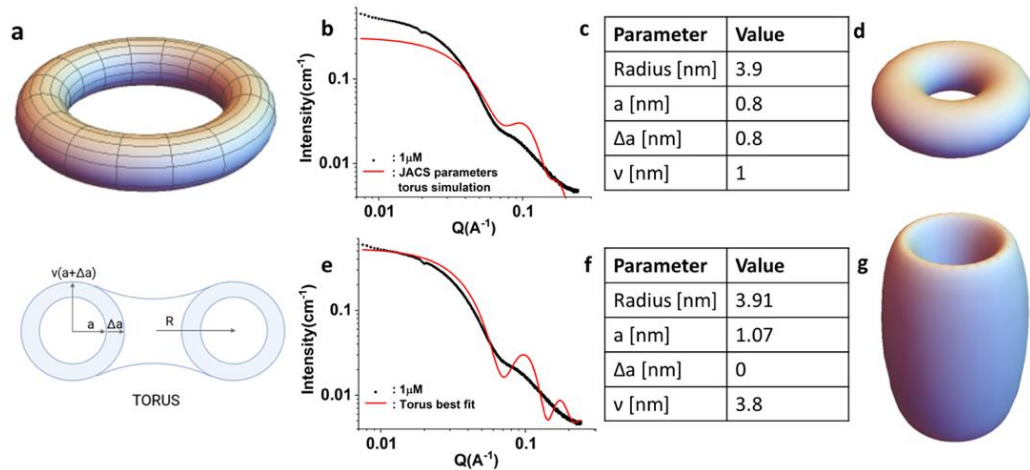


Figure 2: (a) Schematic of the torus model and its fit parameters. (b) Fit of experimental SAXS scattering pattern for Sample 1 using fit parameters derived from previous (TEM) studies shown in (c) and associated visual representation in (d). (e) Best fit of SAXS scattering pattern for Sample 1 using the torus model, resulting fit parameters (f), and associated visual representation (g).

To that end, a new hollow cylinder form factor found in SASview (Figure 3a) was considered<sup>44</sup>. Important parameters in the hollow cylinder model include  $r$ ,  $t$ ,  $l$ ,

sld, and  $sld_{\text{solvent}}$ , where  $r$  is the cylinder core radius,  $t$  is the cylinder wall thickness,  $l$  is the cylinder length (or height),  $sld$  is the cylinder scattering length density, and  $sld_{\text{solvent}}$  is the solvent scattering length density. Previous literature has shown that the hollow cylinder form factor is a suitable approximation for torus shaped objects, especially for polydisperse cases<sup>50-51</sup>. Using the hollow cylinder form factor, again an initial curve shown in Figure 3b was generated using parameters from previous TEM studies, which once again provided a poor fit but correctly represented characteristic features of the scattering data like the position, in  $q$ , of the first minimum<sup>33</sup>. This simulation enabled implementation of a distribution in one parameter. To that end, a Schulz polydispersity of 0.195 in the cylinder core radius was used. After optimization starting with the previously-described simulation parameters, a high-quality fit was obtained (Figure 3d).

Parameters from the fit are summarized in Figure 3c, with cylinder core radius of 2.84 nm with a polydispersity of 0.41, a cylinder wall thickness of 2.13 nm, and a length of 8.1 nm, translating to inner radius and diameter of 2.84 nm and 5.68 nm and outer radius and diameter of 4.97 nm and 7.94 nm, respectively, and a height of 8.1 nm. Interestingly, these parameters are largely similar to those given by the monodisperse torus with an elliptical shell fit obtained using SASfit, corroborating the similarities between these two form factors. However, a key difference is that the hollow cylinder form factor could account for size distributions in the radius parameter, introducing a “smoothing over” of the fitted curve and thus yielding an improved fit to the scattering pattern. As such, all

further fitting analysis was performed using the hollow cylinder form factor in SASview.

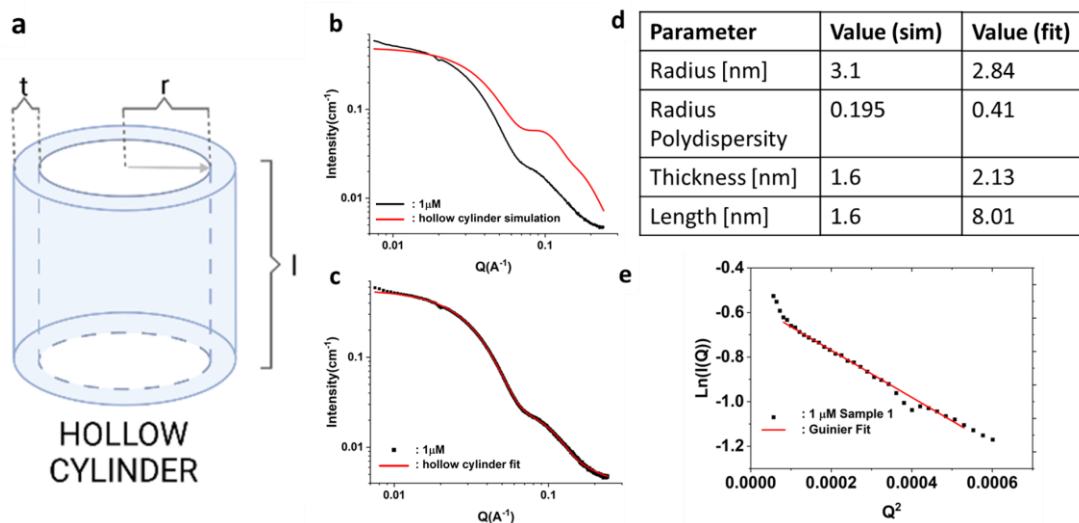


Figure 3: (a) Schematic of the hollow cylinder model and its parameters. (b) Simulation of SAXS scattering pattern of Sample 1 using parameters from previous studies. (c) Best fit using the hollow cylinder model including polydispersity in the radius of the cylinder, with corresponding fit parameters summarized in (d). (e) the Guinier fit of the scattering data of Sample 1.

To confirm results for Sample 1, four more samples of C-rings, which will be referred to as Samples 2, 3, 4, and 5, were analyzed. Samples 2 and 3 followed the same synthesis protocol as that of Sample 1, except that the outer surface was not functionalized with DFO. Samples 4 and 5 additionally deviated from Sample 1 in that the inner surface of the particles was not PEGylated. Table 1 provides the various functionalizations and differences between all samples studied in this report.

Sample	Outer PEGylated	Inner PEGylated	Functionalization
1	X	X	DFO
2	X	X	
3	X	X	
4	X		
5	X		
mC dots	X		
Bimodal	X		
Rings	X		

Table 1: PEGylations and functionalizations of all samples in this report. An ‘X’ shows that the respective sample has that PEGylation or functionalization.

A key question that emerged in the study of these samples was the validity of the fit parameters, especially the height/length parameter, which seemed to be too large when considering the ~2 nm size of primary silica clusters from which the rings are formed<sup>33</sup>. A possible explanation for this unusual height/length is that over time multiple rings in Sample 1, which was synthesized in 2019, had aggregated together resulting in the elongated shape suggested by the fit. This hypothesis is corroborated by the slight upturn in the scattering intensity at low  $q$  observed in the Guinier plot of the data for Sample 1 and deviation from its fit from a Guinier analysis in Figures 3e, which is often a sign of sample aggregation. In order to test whether this behavior is observed in other samples as well, the scattering curves of additional Samples 2-5 were measured and also fitted using the hollow cylinder model. Samples 2 and 3 were only measured at 1  $\mu\text{M}$  concentrations as they were also old samples and there was very little sample left. Samples 4 and 5 were measured at 1, 3, 5, and 10  $\mu\text{M}$  concentrations. The scattering profiles of Samples 4 and 5 for all concentrations are shown in Figure S1. Although higher concentrations lead to better signal to noise ratios, it comes at

the cost of more potential interparticle interaction or aggregation. Scattering data together with their fits from an intermediate concentration of Samples 4 and 5 (5  $\mu\text{M}$  concentration) are compared to those of Samples 2 and 3 (1  $\mu\text{M}$  concentrations) in Figure 4a. As compared to data and fit of Sample 1 in Figure 3d, clearly none of the scattering patterns of these samples new have the upturn at low  $q$  highlighted by a deviation from the fit shown for Sample 1. Once again, the curves all show little oscillations, indicative of a polydisperse sample. Figure 4b shows the Guinier plots for these samples, which all come out to follow linear behavior, irrespective of concentration, suggesting little to no ring aggregation or interactions. Results from fitting of Samples 2-5 are given in Figures 4c-f and associated fit parameters are summarized in Table 2. Comparing values from Samples 2-5 with those from Sample 1, the radius, polydispersity, and thickness parameters are all within the same ballpark with values ranging from 1.6-3.2 nm. The key difference lies in the height/length parameter, where the fit for Sample 1 yielded a value of 8.01 nm whereas those for Samples 2-5 ranged from 5.1-6.5 nm. This difference may be attributed to significant aggregation in Sample 1. The fitted heights of Samples 2-5 are still above the  $\sim 2$  nm expected value for a single ring, however, and its validity will require other characterization techniques to be resolved.

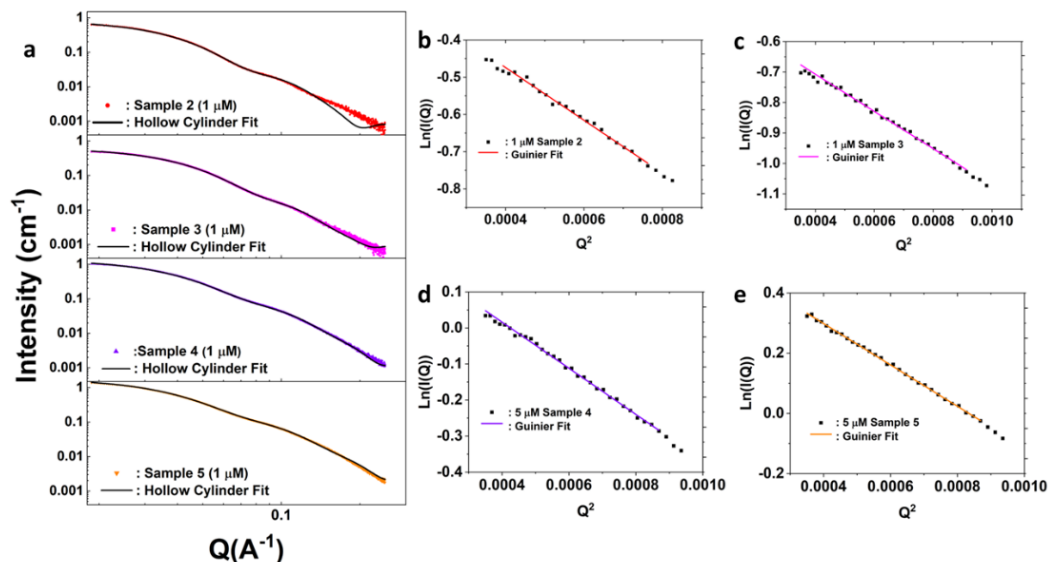


Figure 4: (a) Scattering patterns of Samples 2, 3, 4, and 5 together with their respective fits to a hollow cylinder model. (b-e) Guinier fits of the scattering data of Samples 2-5 as indicated.

Parameter	Sample Number			
	2	3	4	5
Radius [nm]	1.92	1.67	2.19	2.41
Radius Polydispersity	0.48	0.52	0.46	0.45
Thickness[nm]	3.19	3.07	2.59	2.38
Length [nm]	6.50	5.59	5.29	5.12

Table 2: Parameters of the hollow cylinder model derived from fits of experimental SAXS data of Samples 2-5 as shown in Figure 4a.

### 3.2 Validation of Specific SAXS derived Structural Parameters via TEM

To validate ring structural parameters like ring radius and thickness as derived from the fits of the experimental SAXS data sets, TEM images of Samples 2-5 were taken as shown in Figures 5a-d (unfortunately, there was no more sample left after SAXS measurements of Sample 1, and no old TEM images were

available). For data analysis, values were averaged over at least 50 particles (*Methods*). Results of the structural parameters as obtained from TEM image analysis are summarized in Figures 5e-h and compared to the associated parameters from SAXS data fits. In all cases, TEM and SAXS derived inner and outer diameters are very similar. Percent differences between parameters from the two characterization techniques range from ~4-11%, showing good agreement between the two methods.

Interestingly, all outer diameters measured by TEM were smaller than their SAXS counterparts. This can be rationalized by the organic PEG layer not being visible in TEM, as it does not provide enough electron density contrast. Instead, the TEM images only capture the denser silica core of the particles. Although the PEG shell is not accounted for in the hollow cylinder form factor, it is likely that SASview “merged” the scattering contributions from the shell into the core. As the scattering length density of the PEG shell is very low (barely higher than that of the water solvent), it may add a small but noticeable piece to the core thickness and could result in higher diameters than those obtained via TEM analysis. This is supported by comparing inner diameter and thickness values of SAXS and TEM, as shown in Figures 5e-h, in which SAXS inner diameters are consistently smaller than that of TEM and SAXS thicknesses are consistently larger than that of TEM.

Another interesting observation is that the standard deviations for TEM measurements of inner and outer diameter are quite large, while the error bars for

the thicknesses are much smaller. This makes physical sense as there is a lot of deviation among individual particles when it comes to the inner and outer diameters (which are all dependent on the radius in the SAXS models) due to differences in micelle sizes. This is also reflected in the relatively large values of polydispersity for SAXS. However, the thicknesses have smaller deviations between individual particles as most of the walls are composed of one primary silica particle, which is around 1.6-2 nm in size.<sup>33</sup> Although the radius polydispersities at first seem quite different, the values given by SAXS refer to only the inner radius, whereas those given by TEM refer to the entire particle. As such, it is more accurate to compare the two after dividing the values of TEM by 2, in which case the values then become very similar.

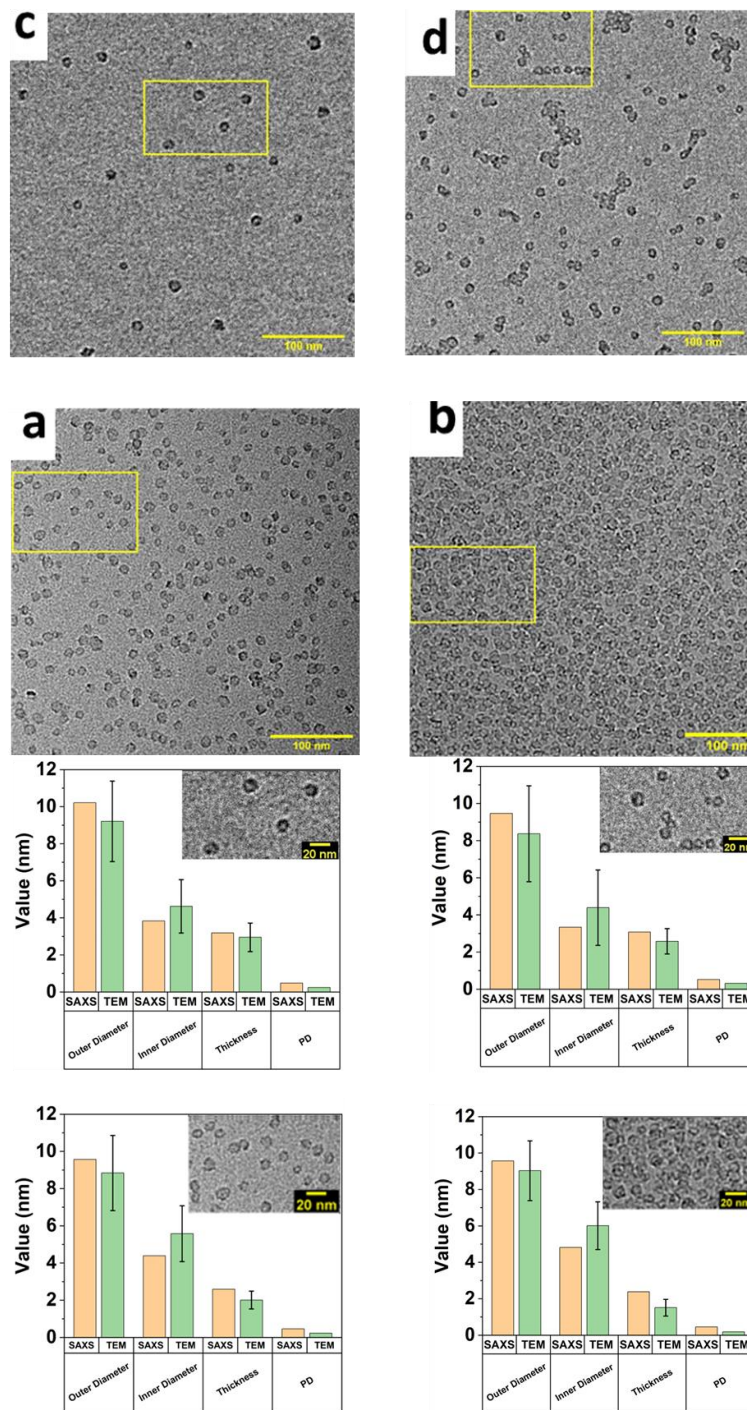


Figure 5: (a-d) TEM images of rings of Samples 2-5. Counts for each sample are  $n = 21$  (a),  $n = 65$  (b),  $n = 197$  (c),  $n = 200$  (d). (e-h) Bar graphs comparing structural parameters for outer diameter, inner diameter, thickness, and polydispersity of Samples 2-5 as obtained from either fits to experimental SAXS data sets (yellow) or from TEM, respectively. Insets in (e-h) show a magnified region of the respective TEM images of the different samples.

Although the SAXS derived radius and thickness parameters have been supported by TEM measurements, the length values which, although are lower in Samples 2-5 than in Sample 1, are still higher than the expected 1.6-2 nm associated with one primary silica cluster forming the rings.

To test the sensitivity of the hollow cylinder model to the length parameter, three additional samples were synthesized with varying TMB concentrations. As shown in previous studies<sup>52</sup>, the concentration of TMB, [TMB], determines the resulting particle morphology. As [TMB] is increased starting from zero, porous silica nanoparticles undergo a bimodal morphology transition from initial pure single-pore mesoporous silica nanoparticles (mC dots) to pure silica rings (C rings), with mixed compositions of mC dots and C rings at intermediate [TMB]. Within the concentration regime exhibiting mixed compositions, while their relative numbers vary, mC dots and C rings exhibit sizes independent of [TMB]. C-rings were shown to be consistently smaller than mC dots in height, which should be reflected in smaller values for the length/height parameter in the model fits<sup>52</sup>. Three TMB concentrations of 0  $\mu\text{M}$ , 50  $\mu\text{M}$ , and 100  $\mu\text{M}$  were used in the synthesis, creating a sample in each region (i.e. pure mC dots, mixed, and pure C rings) and translating to relative molar ratios of 1/0.5/0-1.56 of TMOS/CTAB/TMB. The mC dot sample (synthesized at 0  $\mu\text{M}$  TMB) will be referred to as mC dots, the bimodal sample (synthesized at 50  $\mu\text{M}$  TMB) will be referred to as Bimodal, and the C-ring sample (synthesized at 100  $\mu\text{M}$  TMB) will be referred to as Rings. An additional plot of sample morphology as a function of

TMB concentration and delineating exact TMB concentration values for mC dots, Bimodal, and Rings is provided in Figure S2a.

Scattering curves for the three samples at 5  $\mu\text{M}$  concentrations are compared in Figure 6a (additional curves at concentrations of 1 and 10  $\mu\text{M}$  are provided in Figure S2b-d). There is a noticeable difference between the three curves, especially in the mid  $q$  region, which is the region most impacted by the shape of the samples. Performing model-independent pair distance distribution function calculations on the scattering patterns yields information about the general shape of the particles and provides an  $r^2$  weighted histogram of electron pair distributions in the sample. From the pair distance distribution function curve of the samples (Figure S3a-c), as the particle structure becomes more ring-dominant (from left to right), the corresponding  $P(r)$  curve becomes less right skewed, which is a feature that is indicative of elongated structures, supporting the shortening of hollow cylinders as samples became more ring-dominant. Additionally, looking at these plots from the three different samples suggests that the Bimodal curve looks like a combination of the mC dot and Ring curves, suggesting that it is indeed composed of a mixture of both morphologies. The average electron pair distance also decreases from 7.3 nm to 7.2 nm to 6.5 nm as the morphology transitions from single pore-type particles to rings. Unfortunately, due to the polydispersity in the samples, smaller features in the curve have been “broadened out”, and further information about the structure of the particles cannot be accurately gleaned from the pair distance distribution plots.

Next, fits of the SAXS traces for the three samples were performed as shown in Figures 6b-d. These samples were measured at the same concentration of 5  $\mu\text{M}$  and all three fits were performed using the hollow cylinder model in SASview<sup>44</sup>. While the fits for the ring and bimodal samples have a very low chi-squared value and represent the scattering curve throughout the entire  $q$  region, the single pore sample fit experiences noticeable deviations from the scattering data at intermediate to high  $q$  values. This indicates that the hollow cylinder form factor does not entirely capture the structure of the single-pore nanoparticles. The observed differences in the fit quality may be attributed to the distinction between the C-rings and single-pore nanoparticles, as shown in the models given in Figures 2g and 2a. When compared to a hollow cylinder with straight walls (Fig 2a), the mC dots are expected to have more curved walls. Interestingly, although the fit for the single-pore sample deviates the most from the experimental scattering pattern, the bimodal sample, which contains both single pore and C ring structures, is fit well with the hollow cylinder model. This suggests that as perhaps expected, this type of SAXS analysis is not particularly sensitive to details of the structure in cases where one has an experimental system with mixed sample structures and polydispersity.

Results of the fitting parameters are summarized in Table 3. Sample radii increase from  $\sim 2.1$  nm (single pore) to  $\sim 2.6$  nm (rings), the thickness varies between  $\sim 2.7$  nm (single pore) to  $\sim 2.2$  nm (bimodal), and the length decreases from  $\sim 14.8$  nm

(single pore) to 6.1 nm (rings). The trends for both radius and length as a function of increasing [TMB] are as expected as the particles become wider and shorter as they transitioned from single-pore to ring structures synthesized in the absence or presence of a pore expander molecule (i.e. TMB). Absolute C ring radius and thickness values fall within the range from previous TEM studies, which reported a radius of  $3.1 \pm 0.6$  nm and thicknesses of  $2 \pm 0.6$  nm<sup>33</sup>.

The length/height parameter trend obtained from SAXS data fits suggests that the hollow cylinder model is sensitive to this parameter across the three samples. The output length/height parameters are again larger than expected and previously reported ( $1.6\text{-}2$  nm)<sup>33</sup>. While particle aggregation would provide a rationale for this result, Guinier plots of all three samples show linear behavior (Figure 6e-g), suggesting little, if any, particle aggregation or interparticle interactions, i.e. good single particle data quality. The Guinier fits calculated by BioSAXS RAW also provided radius of gyration values around 5.9 nm, 5.8 nm, and 4.9 nm for mC dot, Bimodal, and Ring samples, respectively<sup>45</sup>. Model-dependent Rg values are calculated using SAXS-derived fit values to compare with the model-independent Rg values provided by BioSAXS RAW and yield similar values with the same trend, further corroborating SAXS fit parameters (see SI for more information). The trend of decreasing radius of gyration as the nanoparticle structures transitioned from single pores to rings is consistent with decreasing size (length/height) as provided by SAXS form factor fits.

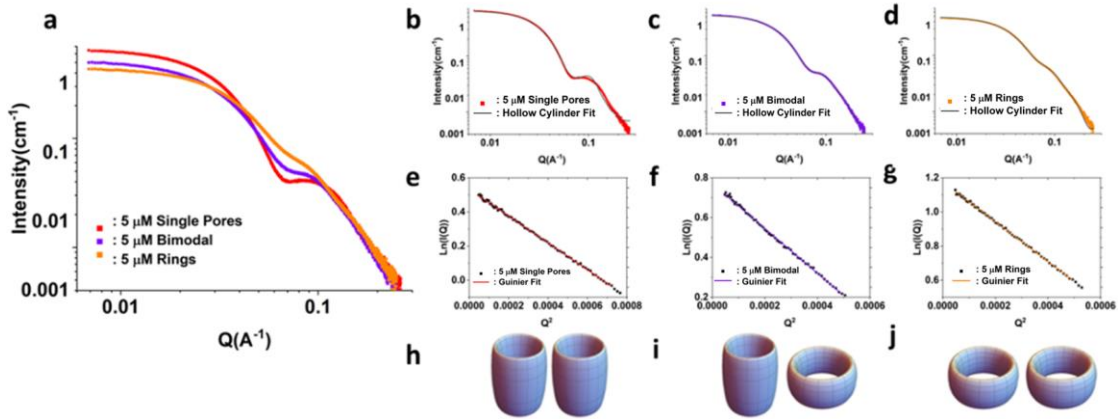


Figure 6: (a) Scattering patterns for single pore, bimodal, and ring samples, which differ in [TMB] used in their synthesis (see main text). (b-d) Experimental SAXS data sets shown in (a) together with their respective fits using the hollow cylinder model for mC dots, Bimodal, and Rings, respectively. (e-g) Guinier fits to the scattering data of mC dots, Bimodal, and Rings, respectively. (h-j) Schematics of the structure of mC dots, Bimodal, and Rings, respectively, as suggested from fit parameters.

	Sample		
	Single Pores	Bimodal	Rings
<b>SAXS Parameter</b>			
Radius [nm]	2.07	2.54	2.64
Radius Polydispersity	0.29	0.47	0.38
Thickness [nm]	2.67	2.22	2.55
Length [nm]	14.83	10.0	6.11
<b>Guinier Parameter</b>			
Radius of Gyration [nm]	5.91	5.81	4.86

Table 3: Table summarizing relevant parameters of mC dots, Bimodal, and Rings from both SAXS data fitting and model-independent Guinier fits.

Closer inspection of TEM images of mC dots can be used to corroborate the increased particle length, as illustrated in Figure 7a and a magnification in the inset of Figure 7b. From this image, hollow cylinders that are laying down are observed as two dark parallel lines separated by a region of very low contrast. The two parallel lines can be interpreted as the side walls of the cylinder when it is laying down and the middle region as the hollow space in between the walls.

Although the middle region also includes the upper and lower walls in the cylinder (where the lower wall is the “floor” of the cylinder that is contacting the TEM grid), this region displays a smaller cross section across silica domains, resulting in very light contrast. To better observe some of these laying down hollow cylinders, the highlighted area in Figure 7b show specific examples that are circled in yellow. Figure 7b also provides a comparison of SAXS and TEM derived structural length scales, showing that the outcomes of the two techniques are in good agreement with each other when such structures are taken into account. From the inset in Figure 7b and the error bar for the length parameter, it is clear that there is large disparity in the length. Indeed, from the histogram of the measured lengths (Figure 7c), there is a right-skewed distribution. Although both SAXS and TEM give average particle lengths of nearly 15 nm, the distribution shows that the majority of particles range from 8-15 nm in length with most of them in the 11-12 nm region. However, the presence of especially elongated cylinders going up to nearly 30 nm brings the average length up to 15 nm.

Analyzing the TEM image of the Bimodal sample (Figure S4a) also shows a clear presence of both rings and mC dots, which can be observed as both being standing up or laying down. To differentiate between rings and standing-up mC dots, rings typically have lighter contrasts in their silica shell and have larger thicknesses and consequently lower radii. Additionally, mC dots can adopt star-shaped morphologies whereas rings are mostly circular or elliptical. TEM image of the

Ring sample and its analysis and comparison to SAXS measurements are shown in Figure S4b, c.

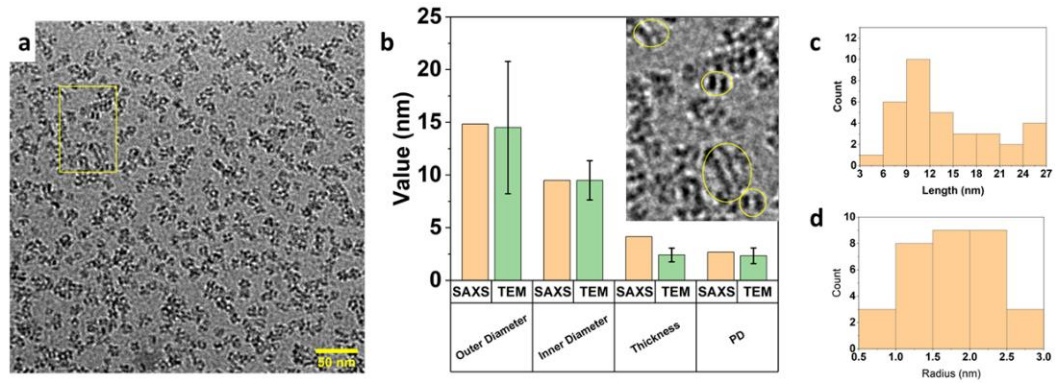


Figure 7: (A) TEM image of mC dots. (b) Bar graph comparing TEM and SAXS derived parameters of length/height, outer and inner diameter, and thickness of mC dots. The inset in (b) is from the highlighted region (yellow box) in (a). Circles are drawn to emphasize examples consistent with laying-down cylinders. (c) and (d) are histograms of the length/height and radius, respectively, as measured from the image in (a).

## CHAPTER 4

### CONCLUSION

In this study, size and size dispersity of C-rings and mC dots were quantitatively measured using SAXS. Key parameters that could be determined were the radius, radius polydispersity, thickness, and length. It was found that the two morphologies have more elongated shapes than what was previously thought, which could be supported additional TEM measurements.

Inspired by the results of this study, future work might include experimental SAXS analysis of further silica nanoparticle morphologies such as cages.<sup>32,33</sup> In addition, although the hollow cylinder model has proven to be a good approximation for the silica structures investigated in this project, it still could be improved by adding an additional shell to account for the outer organic PEG shell, which is hypothesized to just be “absorbed” into part of the silica layer in the SAXS fit. Application of this research could be to use SAXS characterization as a tool alongside clinical applications such as drug delivery or bioimaging to determine, e.g., size cutoffs for favorable biodistributions and renal clearance of nonspherical particles.

## CHAPTER 5

### SUPPLEMENTARY INFORMATION

The 1-D scattering intensity of a hollow cylinder is calculated in SASView using:

$$P(q) = (scale)V_{shell}\Delta\rho^2 \int_0^1 \Psi^2[qz, R_{outer}(1-x^2)^{1/2}, R_{core}(1-x^2)^{1/2}] \left[ \frac{\sin(qHx)}{qHx} \right]^2 dx$$

$$\Psi[q, y, z] = \frac{1}{1-\gamma^2} [\Lambda(qy) - \gamma^2\Lambda(qz)]$$

$$\Lambda(a) = \frac{2J_1(a)}{a}$$

$$\gamma = R_{core}/R_{outer}$$

$$V_{shell} = \pi(R_{outer}^2 - R_{core}^2)L$$

$$J_1(x) = (\sin(x) - x\cos(x))/x^2$$

Where *scale* is a scale factor,  $H=L/2$ , and  $J_1$  is the first order Bessel function<sup>46</sup>.

The 1-D scattering intensity of a torus and an elliptical torus shell cross-section is calculated in SASfit using<sup>47</sup>:

$$F_{torus}(Q, \Theta, R, x, v, \Delta\eta) = \int_{R-x}^{R+x} 4\pi r \Delta\eta \frac{J_0(Qr \sin \Theta) \sin(Q\gamma(r) \cos \Theta)}{Q \cos \Theta}$$

$$\gamma(r) = v\sqrt{x^2 - (r - R)^2}$$

$$I_{torus}(Q, \Theta, R, x, v, \Delta\eta) = \int_0^{\pi/2} |F_{torus}(Q, \Theta, R, x, v, \Delta\eta)|^2 \sin \Theta d\Theta$$

$$I_{torus,sh}(Q, R, a, \Delta a, v, \Delta\eta_c)$$

$$= \int_0^{\pi/2} |F_{torus}(Q, \Theta, R, a + \Delta a, v, \eta_{shell})|^2 \sin \Theta d\Theta$$

$$- |F_{torus}(Q, \Theta, R, a, v, \Delta\eta_c)|^2 \sin \Theta d\Theta$$

The radius of gyration of a hollow cylinder is calculated using<sup>53</sup>:

$$R_g^2 = \frac{R_1^2 + R_2^2}{2} + \frac{h^2}{12}$$

Where  $R_1$  is the outer diameter and  $R_2$  is the inner radius. Plugging in SAXS-derived parameters gives model-dependent  $R_g$  values of 5.63, 4.78, and 4.48 nm for the mC dots, Bimodal, and Rings, respectively. Comparing this to model-independent  $R_g$  values from the Guinier fits (see Equation 1) of 5.91, 5.81, and 4.86 nm for the mC dots, Bimodal, and Rings, respectively, shows similar values obtained from the two methods. Interestingly, although the model-dependent and model-independent  $R_g$  values of mC dots and Rings differ by no more than 0.4 nm, the values of Bimodal are separated by almost 1 nm. This could possibly be attributed to the high polydispersity of Bimodal and the existence of two separate morphologies muddying the calculation.

Figures S1 and S2 provide the experimental scattering patterns of samples 3 and 4 at 1, 3, 5, and 10  $\mu\text{M}$  concentrations and of the Rings, Bimodal, and mC dots at 1, 5, and 10  $\mu\text{M}$  concentrations. From all of the plots, it is clear that at 1 and 3  $\mu\text{M}$ , the data is noisier at higher  $q$  values above 0.2. However, once the concentration reaches 5  $\mu\text{M}$ , the signal to noise ratio drastically improves even in the high  $q$  regions. As such, the 5  $\mu\text{M}$  data sets were chosen to be analyzed in this study. Additionally, Figure S2a provides SASview fit hollow cylinder lengths at [TMB] synthesis condition of mC dots, Bimodal, and Rings and displays [TMB] regions which lead to mC dot, bimodal, and ring samples.

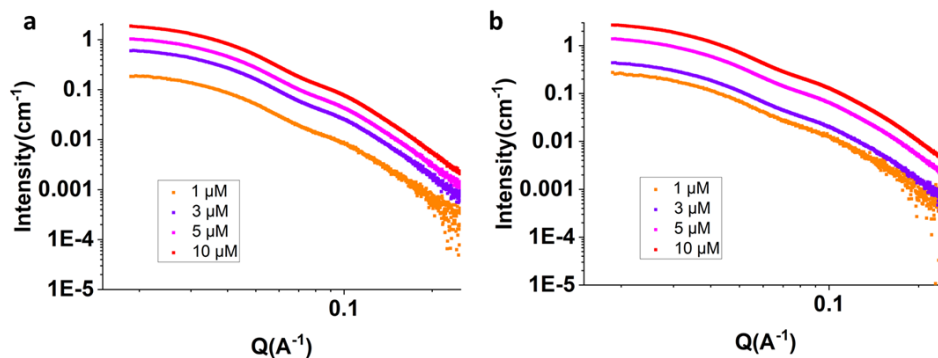


Figure S1: (a-b) Experimental scattering patterns of Samples 4 and 5 at 1, 3, 5, and 10  $\mu\text{M}$ , respectively. For both samples, the 5  $\mu\text{M}$  curve was used for all analyses shown in this project as it was the lowest concentration where there is little noise at higher  $q$  values.

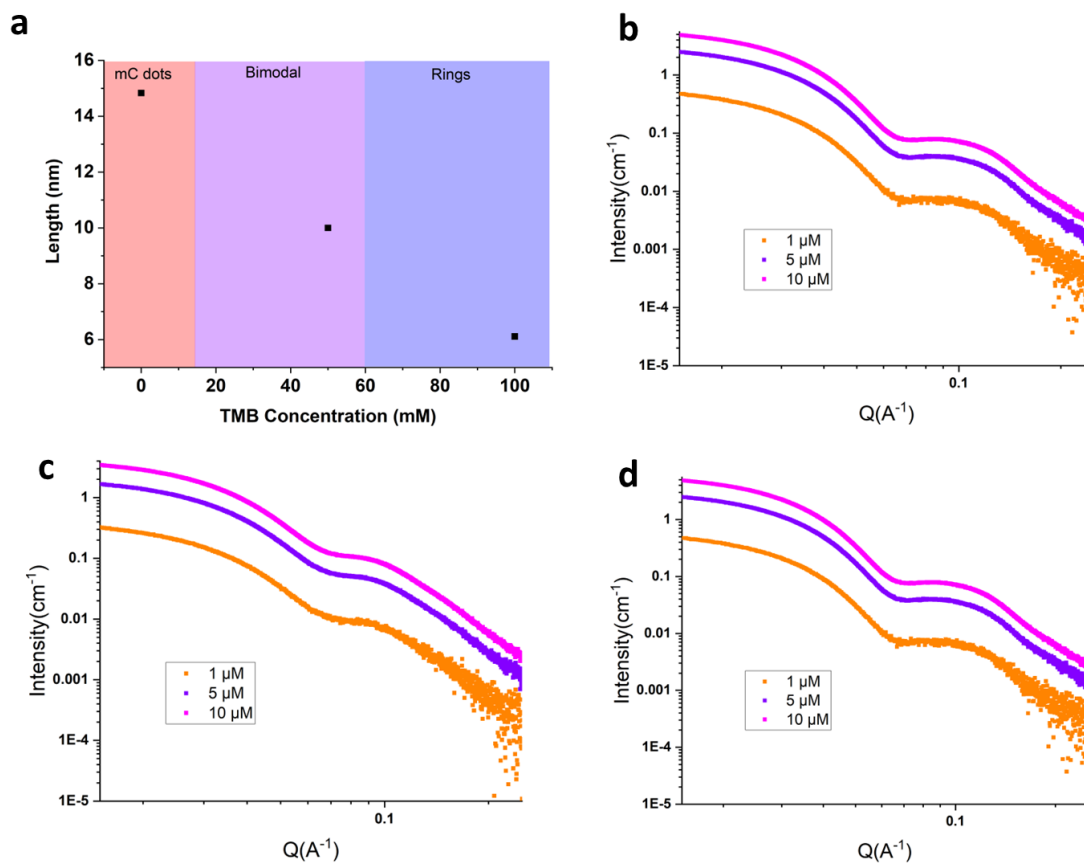


Figure S2: (a) Hollow cylinder length determined by SAXS for mC dots, Bimodal, and Rings. The three colored regions display the sample morphology as a function of TMB concentration. The three points represent the exact TMB concentration used to synthesize mC dots, Bimodal, and Rings. (b-d) Experimental scattering patterns of mC dots, Bimodal, and Rings, respectively, at 1, 5, and 10  $\mu\text{M}$ .

Figure S3 illustrates the  $P(r)$  plots for SAXS data of mC dots, Bimodal, and Ring samples, as well as of ring Sample 4 and 5. It is observed that as  $[TMB]$  increases (from mC dots to Rings) and the sample becomes more ring-dominant, the corresponding  $P(r)$  plot becomes less right skewed, suggesting decreasing particle sizes. Additionally, the  $P(r)$  plot of the Bimodal sample appears to be a combination of the  $P(r)$  plots of mC dots and Rings, suggesting that it has subpopulations from both single pore and ring morphologies. Figure S3d-e are the  $P(r)$  pots for Samples 4 and 5, which are pure ring samples and indeed are very similar to the  $P(r)$  plot for Rings (Figure S3c).

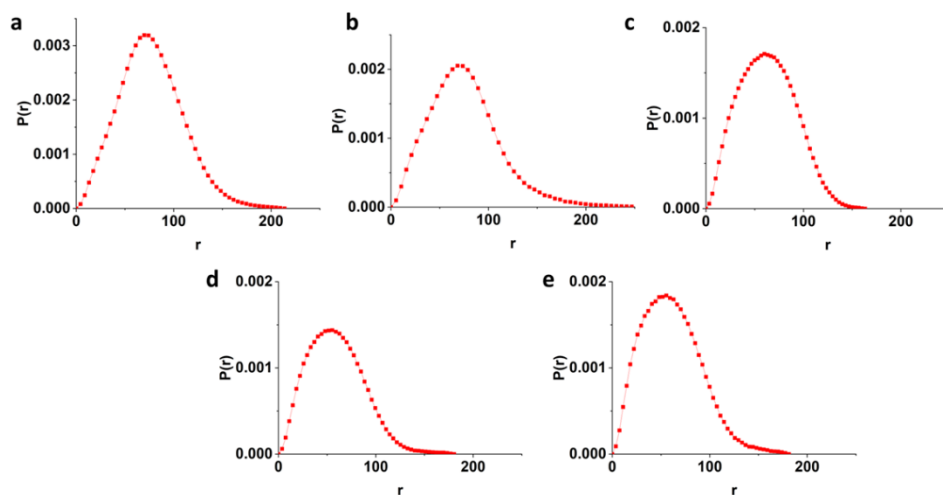


Figure S3: (a-e) Pair distance distribution function analyses of mC dots, Bimodal, Rings, Sample 4, and Sample 5, respectively. Note that Samples 4 and 5 are pure silica rings as well.

TEM analysis of the Bimodal sample displays both rings and mC dots. While all rings are observed in the standing up position, mC dots can be seen as cylinders that are laying down and as cylinders that are standing up. Some examples of all three configurations are highlighted in Figure S4a where rings are shown using

green arrows, laying down cylinders using yellow arrows, and standing-up cylinders using red arrows. Figure S4b is a TEM image of the Ring sample and Figure S4c shows its analysis and comparison to values derived from the analysis of SAXS data using the hollow cylinder model.

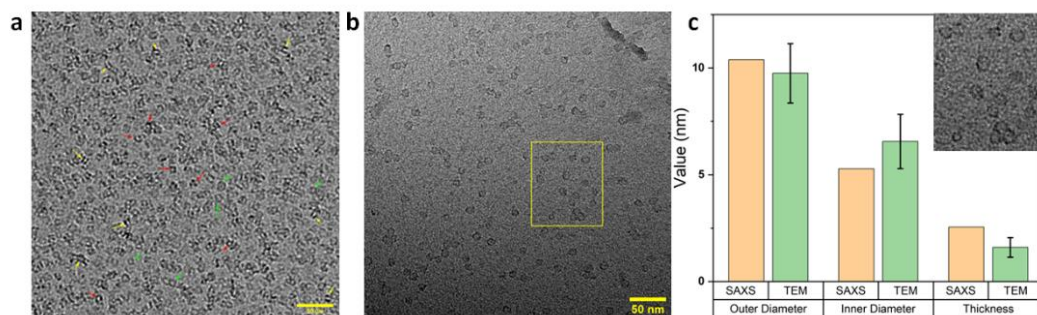


Figure S4: (a) TEM image of Bimodal where both rings and mC dots that are laying down and standing up are visible. Rings are highlighted by green arrows, laying down mC dots are highlighted by yellow arrows, and standing up mC dots are highlighted by red arrows. (b) TEM image of Rings with (c) measurements of inner and outer diameter and thickness and comparisons to parameters derived from SAXS analysis. The highlighted region in (b) is shown as an inset in (c).

## REFERENCES

1. Zarschler, K. *et al.* Ultrasmall inorganic nanoparticles: State-of-the-art and perspectives for biomedical applications. *Nanomedicine Nanotechnology, Biol. Med.* **12**, 1663–1701 (2016).
2. Ehlerding, E. B., Chen, F. & Cai, W. Biodegradable and renal clearable inorganic nanoparticles. *Adv. Sci.* **3**, 1–8 (2015).
3. Heneweer, C., Gendy, S.E.M., Penate-Medina, O. Liposomes and inorganic nanoparticles for drug delivery and cancer imaging. *Ther. Deliv.* **3**, 645–656 (2012).
4. Jaque, D. *et al.* Inorganic nanoparticles for optical bioimaging. *Adv. Opt. Photonics* **8**, 1 (2016).
5. Li, Z. *et al.* Ultra-small fluorescent inorganic nanoparticles for bioimaging. *J. Mater. Chem. B* **2**, 2793–2818 (2014).
6. Phillips, E. *et al.* Clinical translation of an ultrasmall inorganic optical-PET imaging nanoparticle probe. *Sci. Transl. Med.* **6**, 1–10 (2014).
7. Kharisov, B. I., Dias, H. V. R., Kharissova, O. V. & Vázquez, A. Ultrasmall particles in the catalysis. *J. Nanoparticle Res.* **16**, (2014).
8. Bai, X., Wang, J., Mu, Q. & Su, G. In vivo Protein Corona Formation: Characterizations, Effects on Engineered Nanoparticles' Biobehaviors, and Applications. *Front. Bioeng. Biotechnol.* **9**, 1–16 (2021).
9. Suk, J.S. *et al.* PEGylation as a Strategy for Improving Nanoparticle-based Drug and Gene Delivery. *Adv. Drug Deliv. Rev.* **99**, 28–51 (2016).

10. Jokerst, J. V., Lobovkina, T., Zare, R. N. & Gambhir, S. S. Nanoparticle PEGylation for imaging and therapy. *Nanomedicine* **6**, 715–728 (2011).
11. Ma, K. *et al.* Control of Ultrasmall Sub-10 nm Ligand-Functionalized Fluorescent Core-Shell Silica Nanoparticle Growth in Water. *Chem. Mater.* **27**, 4119–4133 (2015).
12. Zanoni, D. K. *et al.* Use of Ultrasmall Core-Shell Fluorescent Silica Nanoparticles for Image-Guided Sentinel Lymph Node Biopsy in Head and Neck Melanoma: A Nonrandomized Clinical Trial. *JAMA Netw. Open* **4**, 1–14 (2021).
13. Phillips, E. *et al.* Clinical translation of an ultrasmall inorganic optical-PET imaging nanoparticle probe. *Sci. Transl. Med.* **6**, 260ra149-260ra149 (2014).
14. Chen, F. *et al.* Ultrasmall targeted nanoparticles with engineered antibody fragments for imaging detection of HER2-overexpressing breast cancer. *Nat. Commun.* **9**, (2018).
15. Chen, F. *et al.* Melanocortin-1 Receptor-Targeting Ultrasmall Silica Nanoparticles for Dual-Modality Human Melanoma Imaging. *ACS Appl. Mater. Interfaces* **10**, 4379–4393 (2018).
16. Aragon-Sanabria, V. *et al.* Ultrasmall Nanoparticle Delivery of Doxorubicin Improves Therapeutic Index for High-Grade Glioma. *Clin. Cancer Res.* OF1–OF15 (2022).
17. Madajewski, B. *et al.* Molecular Engineering of Ultrasmall Silica Nanoparticle-Drug Conjugates as Lung Cancer Therapeutics. *Clin. Cancer Res.* **26**, 5424–5437 (2020).

18. Zhang, X. *et al.* Targeted Melanoma Radiotherapy Using Ultrasmall  $^{177}\text{Lu}$ -Labeled  $\alpha$ -Melanocyte Stimulating Hormone-Functionalized Core-Shell Silica Nanoparticles. *Biomaterials* **241**, (2020).
19. Juthani, R. *et al.* Ultrasmall core-shell silica nanoparticles for precision drug delivery in a high-grade malignant brain tumor model. *Clin. Cancer Res.* **26**, 147–158 (2020).
20. Kohle, F. F. E., Li, S., Turker, M. Z. & Wiesner, U. B. Ultrasmall PEGylated and Targeted Core-Shell Silica Nanoparticles Carrying Methylene Blue Photosensitizer. *ACS Biomater. Sci. Eng.* **6**, 256–264 (2020).
21. Kim, S.E. *et al.* M. Ultrasmall Nanoparticles Induce Ferroptosis in Nutrient-Deprived Cancer Cells and Suppress Tumour Growth. *Nat. Nanotechnol.* **11**, 977–985 (2016).
22. Du, B., Yu, M. & Zheng, J. Transport and interactions of nanoparticles in the kidneys. *Nat. Rev. Mater.* **3**, 358–374 (2018).
23. Burns, A. *et al.* Fluorescent Silica Nanoparticles with Efficient Urinary Excretion for Nanomedicine. *Nano Lett.* **9**, 442–448 (2009).
24. Chen, F. *et al.* Target-or-clear zirconium-89 labeled silica nanoparticles for enhanced cancer-directed uptake in Melanoma: A comparison of radiolabeling strategies. *Chem. Mater.* **29**, 8269–8281 (2017).
25. Ma, K. & Wiesner, U. Modular and Orthogonal Post-PEGylation Surface Modifications by Insertion Enabling Penta-Functional Ultrasmall Organic-Silica Hybrid Nanoparticles. *Chem. Mater.* **29**, 6840–6855 (2017).

26. Kresge, C.T. *et al.* Ordered Mesoporous Molecular Sieves Synthesized by a Liquid-Crystal Template Mechanism. *Nature* **359**, 710–712 (1992).
27. Tang, F., Li, L. & Chen, D. Mesoporous silica nanoparticles: Synthesis, biocompatibility and drug delivery. *Adv. Mater.* **24**, 1504–1534 (2012).
28. Bharti, C., Gulati, N., Nagaich, U. & Pal, A. Mesoporous silica nanoparticles in target drug delivery system: A review. *Int. J. Pharm. Investig.* **5**, 124 (2015).
29. Niculescu, V. C. Mesoporous Silica Nanoparticles for Bio-Applications. *Front. Mater.* **7**, 1–14 (2020).
30. Ma, K., Sai, H. & Wiesner, U. Ultrasmall sub-10 nm near-infrared fluorescent mesoporous silica nanoparticles. *J. Am. Chem. Soc.* **134**, 13180–13183 (2012).
31. Ma, K., Werner-Zwanziger, U., Zwanziger, J. & Wiesner, U. Controlling growth of ultrasmall sub-10 nm fluorescent mesoporous silica nanoparticles. *Chem. Mater.* **25**, 677–691 (2013).
32. Ma, K. *et al.* Self-assembly of highly symmetrical, ultrasmall inorganic cages directed by surfactant micelles. *Nature* **558**, 577–580 (2018).
33. Ma, K. *et al.* Early Formation Pathways of Surfactant Micelle Directed Ultrasmall Silica Ring and Cage Structures. *J. Am. Chem. Soc.* **140**, 17343–17348 (2018).
34. Turker, M. Z. *et al.* Inner and Outer Surface Functionalizations of Ultrasmall Fluorescent Silica Nanorings As Shown by High-Performance Liquid Chromatography. *Chem. Mater.* **31**, 5519–5528 (2019).
35. Barteau, K. P. *et al.* Quantitative Measure of the Size Dispersity in Ultrasmall Fluorescent Organic-Inorganic Hybrid Core-Shell Silica Nanoparticles by Small-Angle X-ray Scattering. *Chem. Mater.* **31**, 643–657 (2019).

36. Chu, B. & Hsiao, B. S. Small-angle X-ray scattering of polymers. *Chem. Rev.* **101**, 1727–1761 (2001).
37. Li, T., Senesi, A. J. & Lee, B. Small Angle X-ray Scattering for Nanoparticle Research. *Chem. Rev.* **116**, 11128–11180 (2016).
38. Kikhney, A. G. & Svergun, D. I. A practical guide to small angle X-ray scattering (SAXS) of flexible and intrinsically disordered proteins. *FEBS Lett.* **589**, 2570–2577 (2015).
39. Ilavsky, J. Nika: Software for two-dimensional data reduction. *J. Appl. Crystallogr.* **45**, 324–328 (2012).
40. Acerbo, A. S., Cook, M. J. & Gillilan, R. E. Upgrade of MacCHESS facility for X-ray scattering of biological macromolecules in solution. *J. Synchrotron Radiat.* **22**, 180–186 (2015).
41. Skou, Soren; Gillilan, Richard. E.; Ando, N. Synchrotron-based Small-Angle X-ray Scattering (SAXS) of Proteins in Solution. *Nat. Protoc.* **9**, 1727–1739 (2014).
42. Svergun, D. I. Determination of the regularization parameter in indirect-transform methods using perceptual criteria. *J. Appl. Crystallogr.* **25**, 495–503 (1992).
43. Petoukhov, M. V, Konarev, P. V, Kikhney, G. & Dmitri, I. ATSAS 2.1 - Supported Small-Angle Scattering Data Analysis. *Appl. Crystallogr.* **40**, s223–s228 (2007).
44. Jacques, D. A. & Trehwella, J. Small-angle scattering for structural biology - Expanding the frontier while avoiding the pitfalls. *Protein Sci.* **19**, 642–657 (2010).

45. Liu, H. & Zwart, P. H. Determining pair distance distribution function from SAXS data using parametric functionals. *J. Struct. Biol.* **180**, 226–234 (2012).
46. Doucet, M., et al. SasView version 4.1.2., 2017.
47. Breßler, I., Kohlbrecher, J. & Thünemann, A. F. SASfit: A tool for small-angle scattering data analysis using a library of analytical expressions. *J. Appl. Crystallogr.* **48**, 1587–1598 (2015)
48. Vrugt, J. A. *et al.* Accelerating Markov chain Monte Carlo simulation by differential evolution with self-adaptive randomized subspace sampling. *Int. J. Nonlinear Sci. Numer. Simul.* **10**, 273–290 (2009).
49. Hollamby, M. J. *et al.* Simultaneous SAXS and SANS Analysis for the Detection of Toroidal Supramolecular Polymers Composed of Noncovalent Supermacrocycles in Solution. *Angew. Chemie - Int. Ed.* **55**, 9890–9893 (2016).
50. Förster, S. *et al.* Fusion of Charged Block Copolymer Micelles into Toroid Networks. *J. Phys. Chem. B* **103**, 6657–6668 (1999).
51. Kumari, H. *et al.* Solution-phase structures of gallium-containing pyrogallol[4]arene scaffolds. *Angew. Chemie - Int. Ed.* **51**, 5086–5091 (2012).
52. Turker, M. Z., Ma, K. & Wiesner, U. Bimodal Morphology Transition Pathway in the Synthesis of Ultrasmall Fluorescent Mesoporous Silica Nanoparticles. *J. Phys. Chem. C* **123**, 9582–9589 (2019).
53. Londono, O.M., et al. Small-Angle X-Ray Scattering to Analyze the Morphological Properties of Nanoparticulated Systems. *Handbook of Materials Characterization*. (2019, Chapter 2).